

---

## CHAPTER 7: TURBULENCE SUPPRESSION AND EMERGING COHERENCE

---

In the previous chapter some experimental questions concerning the different ways how a negative global coupling (NGC) is induced in electrochemical systems were discussed. In this chapter a systematic study of the effect of the NGC on the oscillatory  $\text{Pt}|\text{H}_2\text{SO}_4, \text{Cl}^-$ ,  $\text{Cu}^{2+}|\text{H}_2$  system will be studied. The goal of this chapter is twofold. First, it will be shown that the turbulent regime presented in chapter 5 can be suppressed by imposing some NGC to the system; second, a very rich scenario resulting from the emerging coherence induced by the global constraint will be presented. The results corresponding to the lowest copper

concentration investigated will be presented and discussed in section 7.1. In section 7.2 the effect of the NGC in a system with higher copper concentrations will be discussed. Finally, the main results are summarized in section 7.3.

## 7.1 EXPERIMENTS AT LOW COPPER CONCENTRATION

The results presented throughout this section were obtained using the following electrolyte concentrations: 0.5 mM  $\text{H}_2\text{SO}_4$ , 0.1 mM  $\text{HCl}$ , and 0.01 mM  $\text{CuSO}_4$ . As already mentioned, these conditions are identical to the ones used for the studies in chapter 5 in the absence of NGC. In the following a systematic study of the impact of the NGC upon the dynamics of the system will be presented. The strength of the NGC was varied and results obtained are discussed for increasing coupling strength. Since it has been shown in chapter 6 that the strength of the NGC is proportional to the ratio between the compensated and the cell resistances, the ratio  $R_c/R_\Omega$  will be used as a measure of the NGC strength.

### 7.1.1 RESULTS

#### (a) $R_c/R_\Omega \approx 0.3$ : TWO-PHASE CLUSTERS OF TYPE I

Differently from the other experiments shown at this copper concentration, the results presented in this section were obtained with an adjustable RE (which was mounted in a Haber-Luggin capillary, see chapter 3 for details) that was placed on the axis of the ring WE in a distance of 15 mm of the WE. The ratio  $R_c/R_\Omega$  is a convenient measure of the strength of the NGC. For the experiments described in this subsection,  $R_c/R_\Omega \approx 0.3$ . Moreover, a slightly different electrochemical cell was used in the experiments shown in this section; the details concerning this cell were described in chapter 3.

Five sets of stationary experiments at different applied voltages are shown in Figure 7.1. In the spatiotemporal plots, again only the spatially inhomogeneous part of the data is shown. The first results depicted in Figures 7.1 (a) and (b) were obtained for the lowest applied voltage. The oscillations are relaxation-like, and a sinusoidal structure with wave number 1 popping up on the flanks of the oscillations is observed. Hence, for this low value of  $U$ , the behavior is identical to the one observed without NGC (cf. chapter 5). Similarly to the route observed in case 2 in chapter 5, increasing the applied voltage leads to the

intermittent appearance of traveling structures, which are accompanied by smaller amplitude and higher frequency global current oscillations, c.f. Figures 7.1 (c) and (d).

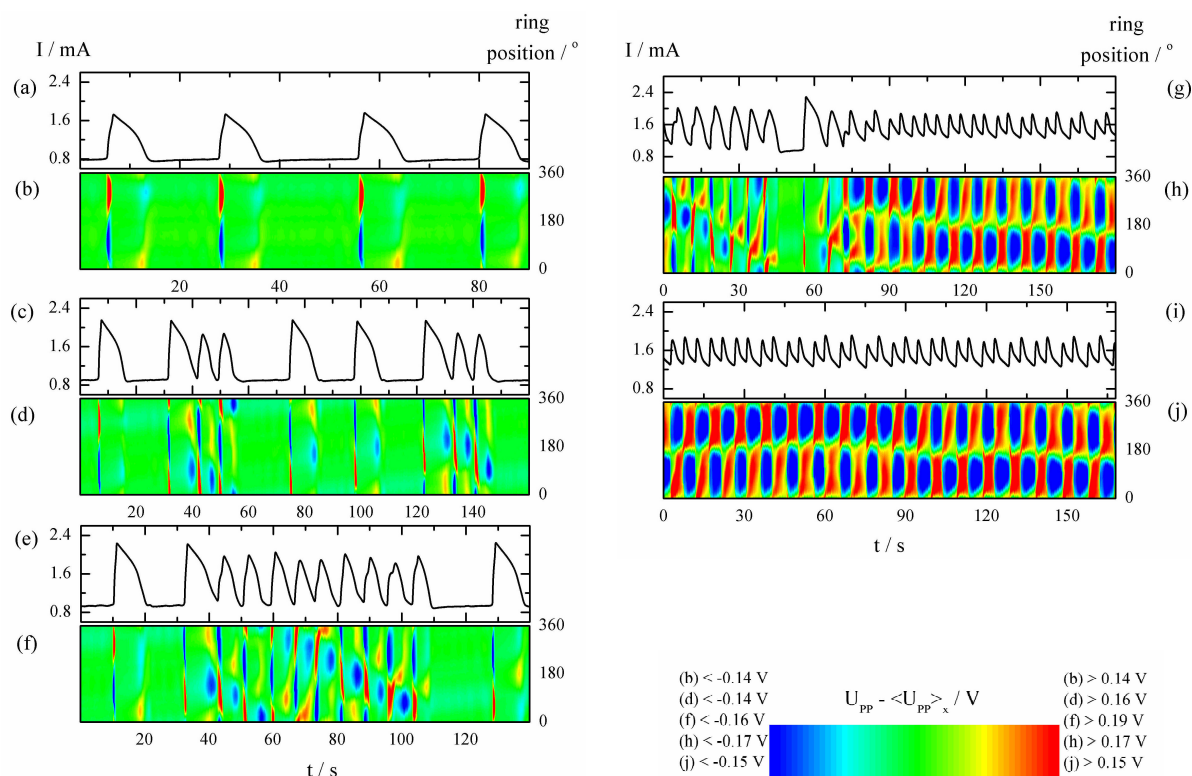


**Figure 7.1:** (a), (c), (e), (g), and (j): Current time series; and (b), (d), (f), (h), and (j): Spatiotemporal evolution of the inhomogeneous part of the interfacial potential,  $U_{PP} - \langle U_{PP} \rangle_x$ , as a function of the ring position and time. Applied voltage  $U$ : (a) and (b): 1.02 V, (c) and (d): 1.11 V, (e) and (f): 1.14 V, (g) and (h): 1.17 V, (i) and (j): 1.18 V. In these experiments a RE mounted in a Haber-Luggin capillary was used and symmetrically placed at a distance of 15 mm from the WE. Under these conditions  $R_c = 160 \pm 10 \Omega$  and since  $R_\Omega = 510 \pm 10 \Omega$ ,  $R_c/R_\Omega \approx 0.3$ . Electrolyte composition: 0.5 mM  $H_2SO_4$ , 0.1 mM HCl, and 0.01 mM  $CuSO_4$ , saturated with  $H_2$ . Rotation rate of the electrode  $\omega = 20$  Hz. A slightly different electrochemical cell was used in these experiments, see chapter 3 for details.

The intermittent appearance of such traveling structures was observed between 1.07 and 1.14 V. It became more often for higher  $U$  values as can be seen in Figure 7.1 (f). But in contrast to the sudden transition into a turbulent regime as observed in the absence of the NGC (case 2 in chapter 5) at even higher voltages, highly ordered anti-phase structures emerged (Figure 7.1 (g)) which were stable upon further increasing the applied voltage (Figure 7.1 (j)). In this state the ring electrode splits into two different domains which oscillate with identical frequency but with a phase shift of  $180^\circ$ . These patterns are usually

referred to as *phase clusters* (or *two-phase clusters*, 2-PCs, in this particular case) and exhibit some resemblance with standing waves. However, in contrast to the latter, cluster patterns are characterized by the absence of an intrinsic spatial wavelength, and their profile tends to be rectangular rather than sinusoidal. Note also that nodal lines separating the two oscillating domains were not strictly stationary. A situation in which each oscillating cluster occupies the same area is usually referred to as phase balance [190]. Figure 7.2 shows a blow-up of the 2-PC patterns shown in Figures 7.1 (i) and (j). In order to distinguish from the 2-PCs shown in the next section, the clusters presented in Figures 7.1 (h) and (j) and Figure 7.2 (b) will be referred from now on as 2-PCs of type I.

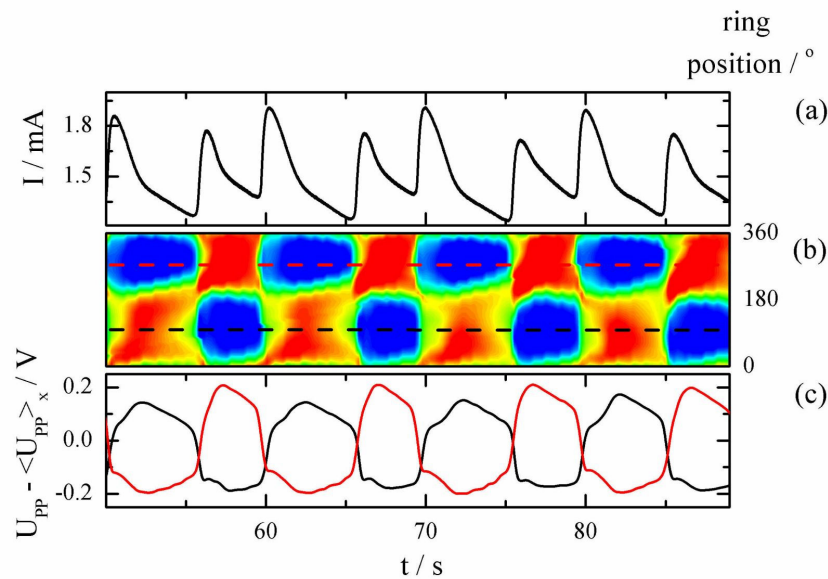


**Figure 7.2:** (a)-(b) corresponds to a blow up of selected regions already given in Figure 7.1 (i)/(j). The local  $(U_{PP}(x) - \langle U_{PP} \rangle_x)/t$  profiles shown in (c) correspond to the positions denoted by the dashed lines in (b). The color scale in (b) is identical to the one given in Figure 7.1 (j), i.e., it ranges from blue to red and corresponds to a potential window from  $-0.15$  to  $0.15$  V.

Additionally to the global current oscillations and the spatiotemporal evolution of  $U_{PP} - \langle U_{PP} \rangle_x$ , depicted in Figures 7.2 (a) and (b), two local time series of  $U_{PP} - \langle U_{PP} \rangle_x$  (taken at positions indicated by the black and red lines in Figure 7.2 (b)) are shown in Figure 7.2 (c). As is seen in Figure 7.2 (b), the domain sizes are not identical. Instead, one covers about 55 % (in the range between 0 and ca.  $200^\circ$ ) and consequently the other one 45 %. As illustrated in the local  $U_{PP} - \langle U_{PP} \rangle_x$  time series in Figure 7.2 (c), the amplitude oscillation of the smaller domain (red lines in Figures 7.2 (b) and (c)) is slightly larger than that in the larger domain. This can be viewed as a consequence of the global constraint that tends to stabilize a situation

in which both domains have the same size. This aspect will be further discussed below. The spatial and temporal asymmetries in the individual cluster dynamics just mentioned are reflected in the differences observed in the amplitude of two successive oscillations of the global current oscillations depicted in Figure 7.2 (a).

The 2-PC patterns were observed up to about  $U = 1.30$  V. At higher applied voltages platinum oxide formation comes into play. In a point-like system it would lead to the annihilation of the limit cycle after its collision with a saddle point in a saddle-loop ('sloop') or homoclinic bifurcation [191]. Figure 7.3 shows three sets of data at different times illustrating the interplay between platinum oxide formation and the oscillatory HOR obtained at  $U = 1.34$  V.

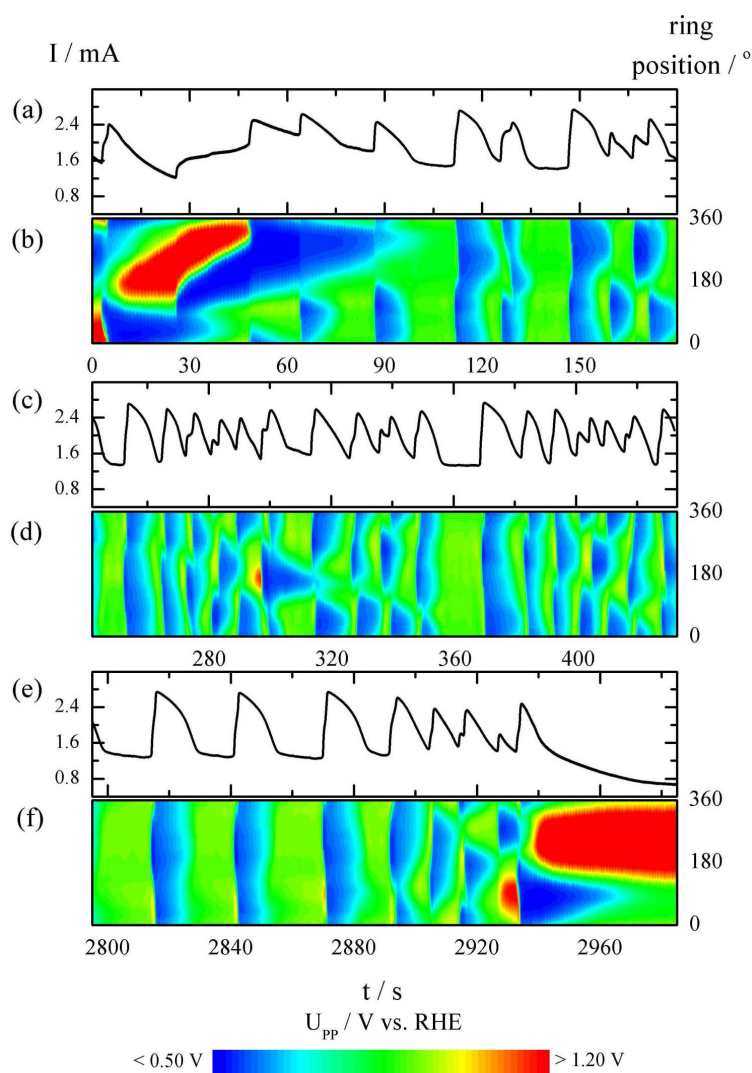


**Figure 7.3:** (a), (c), and (e): Current time series; and (b), (d), and (f): Spatiotemporal evolution of the interfacial potential,  $U_{PP}$ , as a function of the ring position and time. Applied voltage  $U = 1.34$  V and the remaining conditions as in Figure 7.1.

As clearly seen, instead of a sudden transition, expected for a point-like system, the platinum oxide (high potential regions) does not completely cover the surface at once, resulting in a complex transient behavior. Initially an oxide region forms, red domain in Figure 7.3 (b), and tries to expand but, subsequently contracts after some time and finally disappears at ca. 45 s. A behavior similar to that observed at lower applied potentials (cf. Figure 7.1) and apparently without oxide influence is displayed in Figure 7.3 (d). After about 2920 s an oxide domain nucleates again and this time it grows until it occupies the entire surface as is seen Figure 7.3 (f). Stable patterns resulting from the interplay between the oscillatory  $\text{Pt}|\text{H}_2\text{SO}_4, \text{Cl}^-, \text{Cu}^{2+}|\text{H}_2$  system and an oxide covered domain were obtained under different conditions and will be presented in chapter 8.

### (b) $R_c/R_\Omega \approx 0.4$ : TWO-PHASE CLUSTERS OF TYPE II

Results obtained under stronger NGC, namely when  $R_c/R_\Omega \approx 0.40$ , are depicted in Figure 7.4. All results described from here on in this section were obtained employing a negative impedance device (NID) previously described in chapter 6, rather than the adjustable RE.

In Figures 7.4 (a)–(b) typical period-1 (relaxation-like) current oscillations accompanied by sinusoidal spatial structures which are seen in the  $U_{PP} - \langle U_{PP} \rangle_x$  space-time plots are shown. These are qualitatively similar to the structures already shown in Figure 7.1 (a)–(b) and were obtained at the lowest value of  $U$ . At higher applied voltage, period doubled structures are observed and are depicted in Figures 7.4 (c)–(d). Increasing  $U$  further, these structures become unstable, and a transition into cluster-like patterns occurs. Two-phase cluster-like states were observed in the entire voltage interval between 1.20 and 1.55 V and are illustrated in Figures 7.4 (e)–(j). In contrast to results presented in Figure 7.3 above, when increasing even further the applied voltage, a steep transition to the homogeneous (oxide covered) domain takes place and, therefore, no transient pattern in the presence of platinum oxide was observed.

The 2-PCs observed here are less regular than those shown in the previous section. The border motion observed seems to be more pronounced when the asymmetry between the sizes of the two domains increases. This fact is illustrated in Figure 7.4 (h). A clear motion

towards smaller angles is initiated (at ca. 20 s) when the smaller domain shrinks further and seems to cease at about 100 s. Further analysis of this property would require longer time series. In contrast, nearly stationary nodal lines were observed in the case in which phase balance is reached as shown in Figure 7.4 (j).

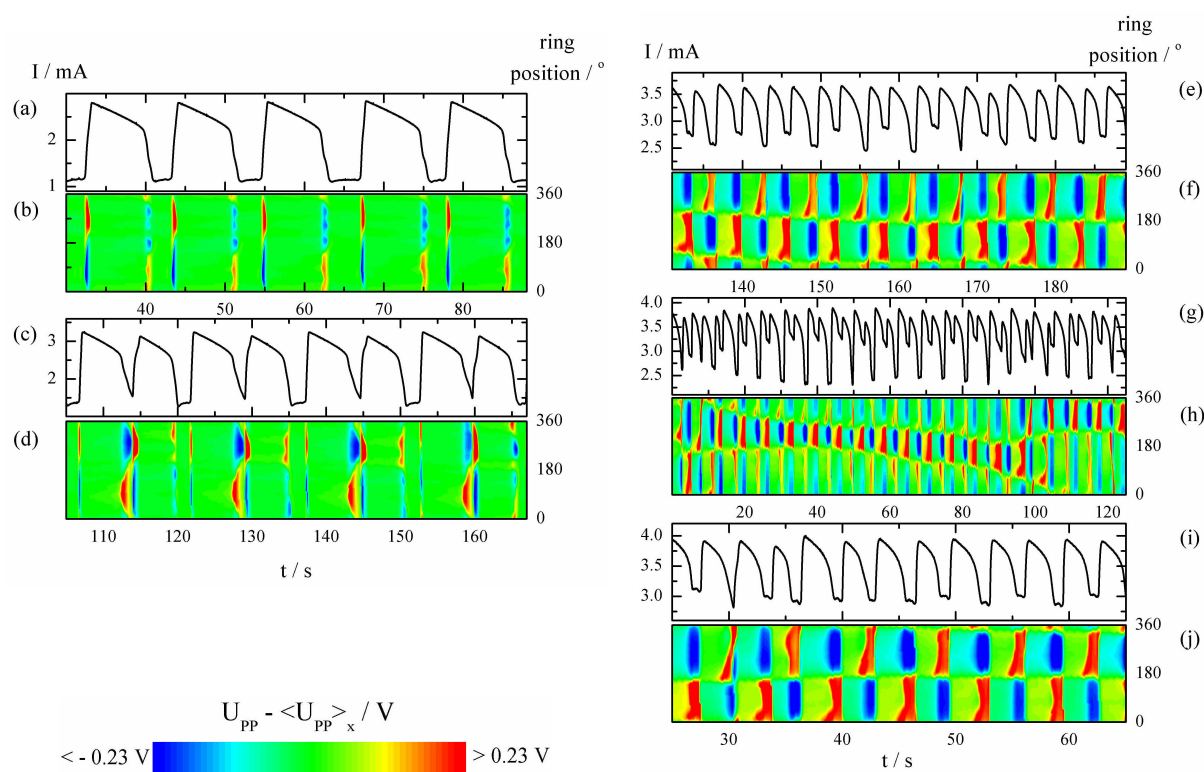


**Figure 7.4:** (a), (c), (e), (g), and (j): Current time series; and (b), (d), (f), (h), and (j): Spatiotemporal evolution of the inhomogeneous part of the interfacial potential,  $U_{PP} - \langle U_{PP} \rangle_x$ , as a function of the ring position and time. Applied voltage  $U$ : (a) and (b): 0.95 V, (c) and (d): 1.04 V, (e) and (f): 1.24 V, (g) and (h) 1.30 V, (i) and (j) 1.34 V. The electrolyte resistance was partially compensated by means of a NID placed between the WE and the potentiostat in such a way that  $R_c = -R_{NID} = 200 \Omega$  and since  $R_\Omega = 490 \pm 10 \Omega$ ,  $R_c/R_\Omega \approx 0.4$ . Electrolyte composition: 0.5 mM  $H_2SO_4$ , 0.1 mM  $HCl$ , and 0.01 mM  $CuSO_4$ , saturated with  $H_2$ . Rotation rate of the electrode  $\omega = 20$  Hz.

Differently from the previous case given in Figure 7.2, the 2-PCs depicted in Figure 7.4 are characterized by the presence of a quiescent or dormant interval in which the interfacial potential amplitude remains nearly constant. In order to discriminate between these two aspects, this second sort of 2-PC will be denoted as type II two-phase clusters.

Figure 7.5 shows a detailed view of the clusters displayed in Figures 7.4 (e)–(f) and (g)–(h). Besides the  $I/t$  (Figures 7.5 (a) and (d)) and  $U_{PP} - \langle U_{PP} \rangle_x$  (Figures 7.5 (b) and (e)) plots, also two local  $(U_{PP} - \langle U_{PP} \rangle_x)/t$  profiles are depicted in Figures 7.5 (c) and (f) for each case.

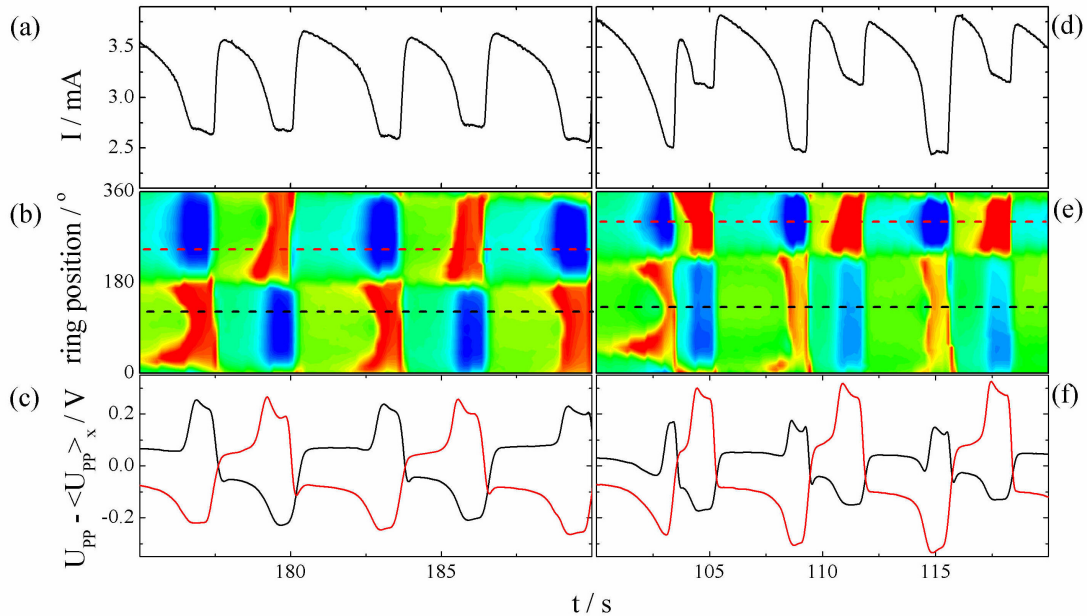


**Figure 7.5:** Data in (a)–(b) and (d)–(e) represent a blow up of selected regions of Figure 7.4 (e)–(f) and (g)–(h), respectively. The local  $(U_{PP} - \langle U_{PP} \rangle_x)/t$  profiles shown in (c) and (f) corresponds to the positions denoted by the dashed lines in (b) and (e), respectively. The color scale in (b) and (e) is identical to the one given in Figure 7.4, i.e., it ranges from blue to red, corresponding to a potential interval of 0.46 V.

In the first situation, Figure 7.5 (b), the areas occupied by different cluster domains are nearly identical, whereas in the second case, Figure 7.5 (e), a larger domain occupies about 2/3 of the electrode area. This asymmetry is clearly perceived in the global current oscillations shown in Figures 7.5 (a) and (d). Note that as in the case of 2-PC of type I shown in Figure 7.2, the larger domain in Figure 7.5 (e) oscillates with smaller amplitude than the smaller domain. This difference becomes more apparent when comparing the local  $(U_{PP} - \langle U_{PP} \rangle_x)/t$  profiles shown in Figures 7.5 (c) and (f). Owing to the comparatively large difference in amplitudes observed in the case displayed in Figure 7.5 (f), these clusters could be classified as *amplitude* rather than *phase* clusters since not only the phase but also the amplitude differs between different domains.

**(c)  $R_c/R_\Omega \approx 0.5$ : IRREGULAR CLUSTERS**

Increasing the strength of the NGC further, the two-cluster structures observed so far break up into more irregular, but still clustered states. For a  $R_c$  to  $R_\Omega$  ratio of about 0.5 such irregular patterns were found along the entire voltage range investigated ( $0.82 \text{ V} < U < 1.45 \text{ V}$ ). The irregular clusters (ICs) observed in this entire voltage region can be further differentiated into two different types. The first kind of irregular motion is illustrated in Figure 7.6. The long-term evolution shown in Figure 7.6 (a) evidences a pronounced drift in the nodal line associated with changes in the size of the clusters. Just as observed above, smaller domains oscillate with higher amplitude. Characteristic of this first kind of ICs is the fact that the electrode is divided into two different regions: one in which smaller clusters of similar sizes coexist, and a second domain in which a single larger cluster oscillates with smaller amplitude. As in the case shown in Figure 7.5 (e), one could speak of amplitude clusters owing to the pronounced difference in the amplitude between large and small domains. Figures 7.6 (b) and (c) show in more detail part of the dynamics depicted in Figure 7.6 (a). The largest domain shown in Figure 7.6 (b) covers somewhat more than half of the surface, and the two smaller neighbor clusters are found in the remaining domain. Increasing the applied potential, the domain filled with the smaller clusters seems to increase on the expense of the other one. Results obtained at  $U = 1.04 \text{ V}$ , i.e.,  $0.1 \text{ V}$  more positive than in Figures 7.6 (a)-(c), are displayed in Figures 7.6 (d) and (e). Instead of two, now three small clusters populate one of the two domains.

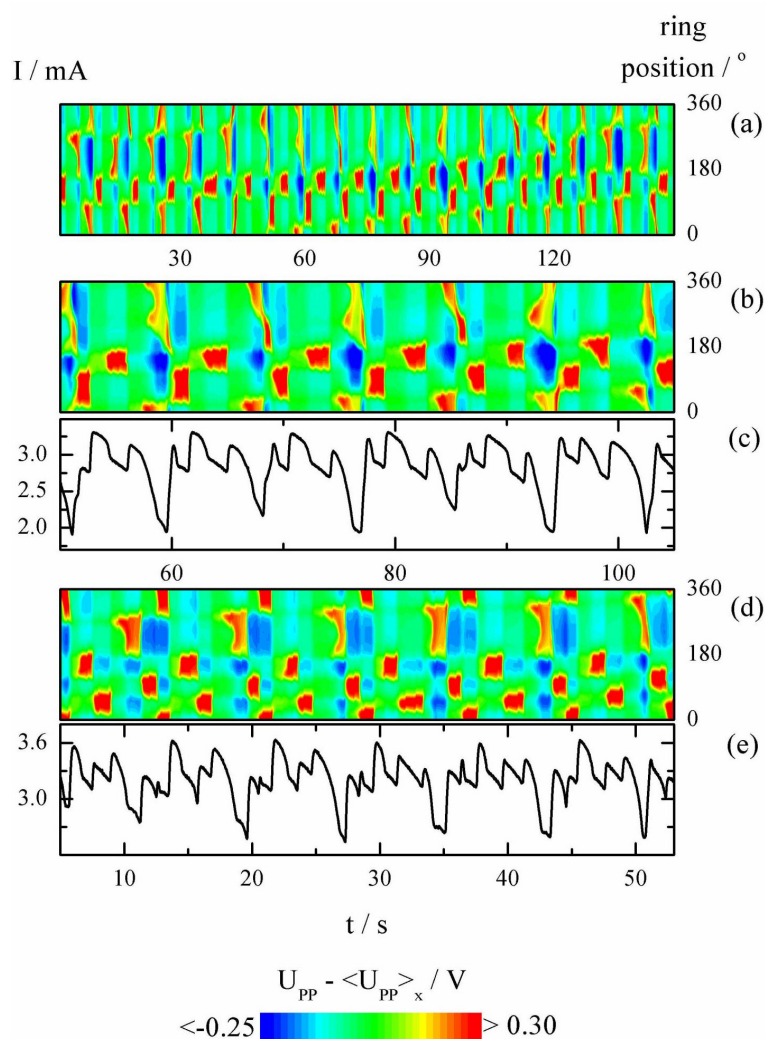


**Figure 7.6:** (a), (b), and (d): Spatiotemporal evolution of the inhomogeneous part of the interfacial potential,  $U_{PP} - \langle U_{PP} \rangle_x$ , as a function of the ring position and time; and (c) and (e): Current time series. Applied voltage  $U$ : (a), (b) and (c): 0.94 V, (d) and (e): 1.04 V. The electrolyte resistance was partially compensated by means of a NID placed between the WE and the potentiostat in such a way that  $R_c = -R_{NID} = 250 \Omega$  and since  $R_\Omega = 490 \pm 10 \Omega$ ,  $R_c/R_\Omega \approx 0.5$ . Remaining conditions identical to those given in Figure 7.4.

When increasing the applied voltage, a continuous transition to a second type of irregular cluster-like motion is observed (Figure 7.7). In this case, the individual clusters change their shapes and positions randomly. This irregular cluster distribution is also reflected in the current time series, as can be seen in Figures 7.7 (b) and (d). The time series are more complex than the ones observed at lower applied voltages, cf. Figures 7.6 (c) and (e).

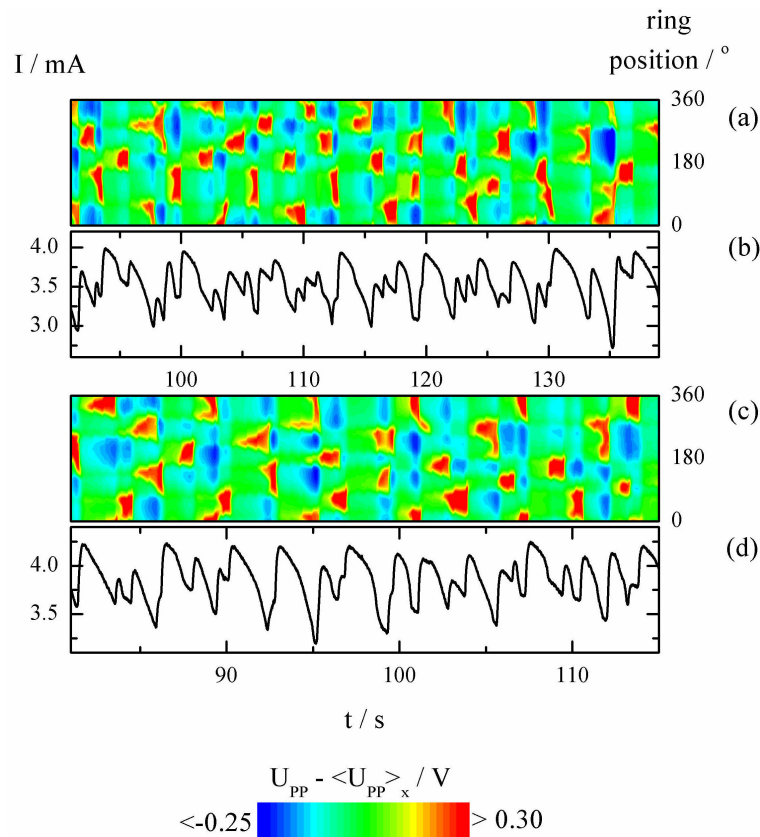


**Figure 7.7:** (a) and (c): Spatiotemporal evolution of the inhomogeneous part of the interfacial potential,  $U_{PP} - \langle U_{PP} \rangle_x$ , as a function of the ring position and time; and (b) and (d): Current time series. Applied voltage  $U$ : (a) and (b): 1.24 V, and (c) and (d): 1.34 V. Remaining conditions identical to the ones given in Figure 7.6.

Although very irregular, the behavior depicted in Figure 7.7 differs significantly from the turbulent regime reported in chapter 5 and the clustered domains observed here are of similar sizes.

#### (d) $R_c/R_\Omega \approx 0.6$ : FIVE-PHASE CLUSTERS

In the presence of stronger NGC, namely when  $R_c/R_\Omega \approx 0.6$ , the irregular motion found in the second type of ICs displayed above turns into highly coherent patterns at higher applied voltages. Irregular clustered states similar to the ICs of the second type depicted in Figure 7.7 were still observed at  $U = 0.85$  V. At  $U$  values of about 0.95 V five-phase clusters emerged. The 5-PCs were observed up to ca. 1.25 V, and typical examples are shown in Figure 7.8.

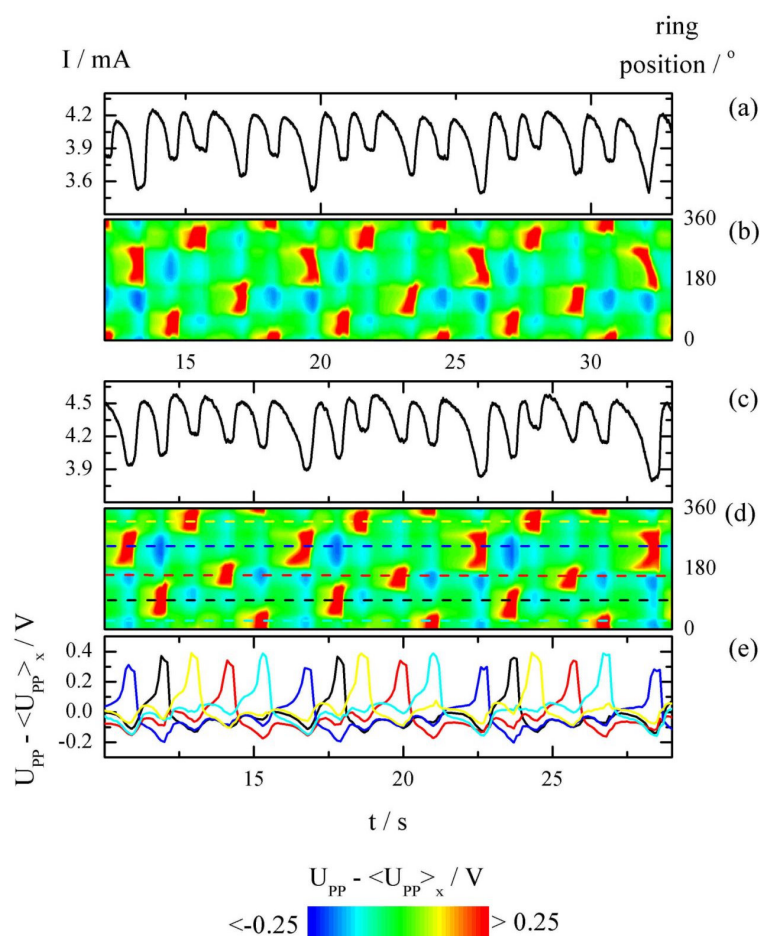


**Figure 7.8:** (a) and (b): Current time series; (b) and (d): Spatiotemporal evolution of the inhomogeneous part of the interfacial potential,  $U_{PP} - \langle U_{PP} \rangle_x$ , as a function of the ring position and time; (e): Local  $(U_{PP} - \langle U_{PP} \rangle_x)$ -t profiles at five different positions as indicated by the dashed lines in (d). Applied voltage  $U$ : (a) and (b): 1.14 V, (c), (d) and (e): 1.24 V. The electrolyte resistance was partially compensated by means of a NID placed between the WE and the potentiostat in such a way that  $R_c = -R_{NID} = 300 \Omega$  and since  $R_\Omega = 490 \pm 10 \Omega$ ,  $R_c/R_\Omega \approx 0.6$ . Remaining conditions identical to those given in Figure 7.4.

Just as in the case of 2-PCs, 5-PCs are characterized by the presence of five different clustered regions that oscillate five times more slowly than the global current does. In this way, each current minimum observed in the  $I/t$  time series displayed in Figures 7.8 (a) and (c) is the result of the passivation of a small portion of the electrode, corresponding to a red domain in space-time plots shown in Figure 7.8 (b) and (d). The relative phases of the oscillations in the five different domains can be easily read off from the local  $(U_{PP} - \langle U_{PP} \rangle_x)/t$  profiles displayed in Figure 7.8 (e). As already mentioned above, in each case the

local oscillation frequency is five times smaller than the oscillation frequency of the global current. Moreover, the rule ‘the larger the domain size, the smaller its oscillation amplitude’ still holds here as is seen in the local  $U_{PP} - \langle U_{PP} \rangle_x$  time series corresponding to the location of the largest cluster domain, cf. the blue line in Figure 7.8 (e).

### (e) $R_c/R_\Omega \approx 0.7$ : PULSES

For even stronger NGC, more precisely for  $R_c/R_\Omega \approx 0.7$ , modulated traveling pulses were observed. Figure 7.8 shows the pulses observed at  $U = 1.04$  V. The pulses seem to be composed of three different domains that are weakly connected and move slowly, cf. Figure 7.8 (a). This feature may be related to a continuous transition from a cluster-like structure and will be further discussed below.

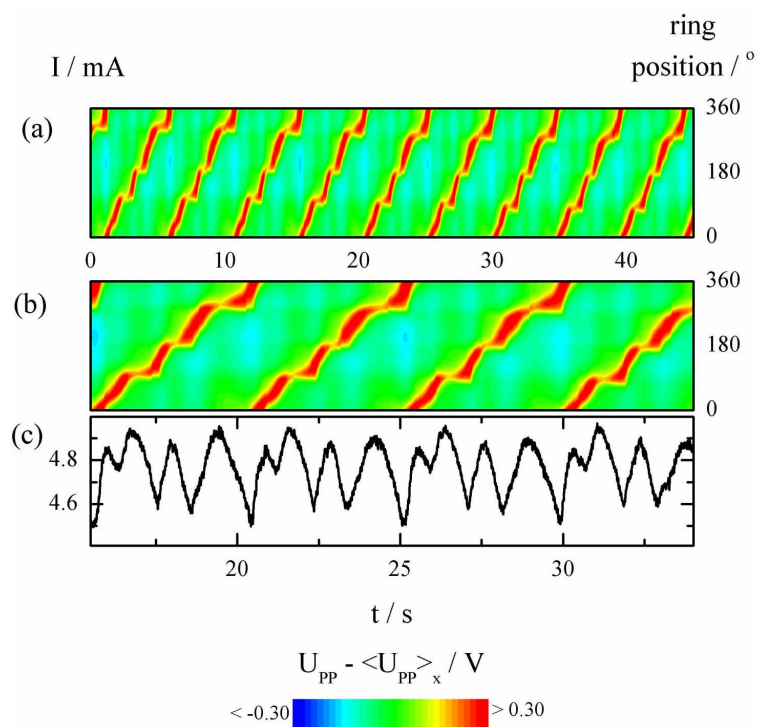


**Figure 7.9:** (a) and (b) Spatiotemporal evolution of the inhomogeneous part of the interfacial potential,  $U_{PP} - \langle U_{PP} \rangle_x$ , as a function of the ring position and time; and (c) Current time series. Applied voltage  $U$ : 1.04 V. The electrolyte resistance was partially compensated by means of a NID placed between the WE and the potentiostat in such a way that  $R_c = -R_{NID} = 350 \Omega$  and since  $R_\Omega = 490 \pm 10 \Omega$ ,  $R_c/R_\Omega \approx 0.7$ . Remaining conditions identical to the ones given in Figure 7.4.

### 7.1.2 DISCUSSION

The collective dynamics of a population of individual oscillators can be viewed as a result of (a) the dynamics of the single elements constituting the system, and (b) the way in which these elements change information among each other. As shown in chapter 5, when subjected to migration coupling, for this electrolyte composition the system undergoes a transition from periodic spatiotemporal oscillations to a turbulent regime for increasing applied voltage. The introduction of a global constraint induces a long range interaction between individual oscillators and, almost independently of the detailed nature of the system in question, synchronization in the collective behavior can be observed from a certain threshold of the strength of the global coupling on. In section 7.1.1 it was demonstrated that already for comparatively weak NGC, turbulence is suppressed and, instead of highly disordered spatiotemporal structures, cluster patterns were found at higher voltages.

Turbulence suppression in spatially extended systems is of great interest both from theoretical and practical points of view. In the context of reacting systems, an empirical method termed time delayed feedback [63, 64] has been successfully used to suppress chemical turbulence during the catalytic CO oxidation on Pt(110) surface [175-177, 192]. Feedback can also be considered as a kind of global constraint and in this specific case, the carbon monoxide partial pressure was used as the control variable in the feedback loop. When increasing the intensity of the global feedback, Ertl and coworkers [175] found transitions from spiral wave turbulence to stable uniform oscillations, including the intermediate sequence: intermittent turbulence→clusters→standing waves.

In contrast to artificial feedback control methods, the global constraint present in electrochemical systems is intrinsic to the operation mode (see refs. [26-28] for up to date reviews) and can be induced either by the galvanostatic operation mode or in the potentiostatic case when part of the cell resistance between the CE and the WE is compensated.

Quite recently, Hudson and coworkers [193] provided experimental evidence of the appearance of coherent dynamics when a certain minimum strength of the global coupling is reached. The experiments were conducted with an array of 64 point-like nickel electrodes coupled via an external resistor. The authors have experimentally proven that when a critical

value of the global constraint is reached, the number of synchronized oscillators continuously increases as predicted by Kuramoto's model [48].

In this section, the dynamics of the system was studied at five different  $R_c/R_\Omega$  ratios, ranging from 0.3 to 0.7. Besides turbulence suppression observed already at  $R_c/R_\Omega \approx 0.3$  and just discussed, a very rich scenario including different cluster-like patterns was found. At  $R_c/R_\Omega \approx 0.3$  and 0.4, modulated oscillations were observed at low applied voltages, and the following sequence was found for increasing NGC strength at high  $U$ : 2-PC (of type I)  $\rightarrow$  2-PC (of type II)  $\rightarrow$  IC  $\rightarrow$  5-PC  $\rightarrow$  Pulses<sup>10</sup>.

Clusters are defined as a group of individual elements oscillating with the same period, phase, and amplitude [194] and are known to arise due to global interactions [195-200]. In contrast to standing waves, clustering or condensation does not imply the existence of an intrinsic wavelength, and also the nodal line separating different domains can evolve in time [199]. In the electrochemical system studied here, different types of clusters were observed.

A careful investigation of phase clusters reported in the literature reveals that some of them are similar to the ones denoted above in this thesis as type I [136] and others resemble the type II clusters [175, 199]. Further insight towards the characterization of the two different types of 2-PC can be given in terms of the Karhunen-Loève Decomposition (KLD). As already mentioned in chapters 2 and 5, the KLD provides a set of basis functions, which are empirically obtained, and the spatiotemporal data are expanded in a series invoking these basis functions. Figure 7.10 shows the KLD of the  $U_{PP}$  signal from which the spatial and temporal average was subtracted (c.f. chapter 2) equivalent to the 2-PC of type I, plate (a), and of type II, plate (b). Shown are the first three more representative modes (or eigenvectors) and their time dependent amplitudes or coefficients. The three modes shown carry about 96 % and 97 % of the information contained in the 2-PCs of types I and II, respectively.

<sup>10</sup> Besides the fact that different patterns can exist in a tiny parameter region, it should be mentioned that when  $R_c/R_\Omega \approx 0.5, 0.6$  and  $0.7$ , the oscillatory region was only partially investigated. Therefore, additional patterns not referred to in this sequence can still exist for different  $U$  values.

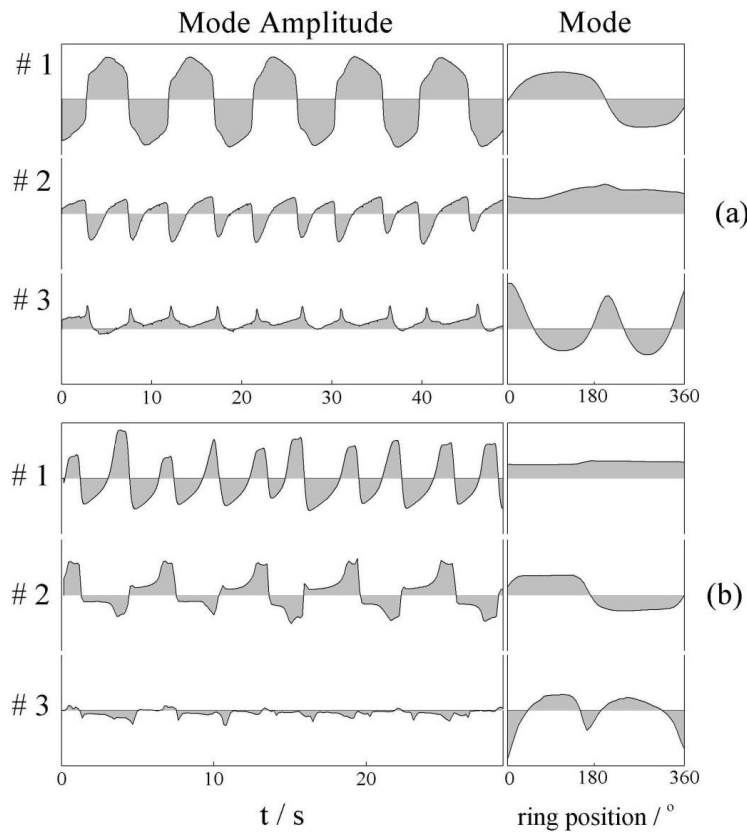


**Figure 7.10:** KLD of the spatiotemporal evolution of the interfacial potential  $U_{PP}$ , corresponding to the 2-PC of (a) type I, and (b) type II. Shown are the first three modes and the corresponding mode amplitudes.

In the case of the 2-PC of type I, Figure 7.10 (a), the cluster-like character is fully captured by the first mode which is responsible for about 80 % of the energy. The second mode is nearly homogeneous and oscillates with the same frequency as the global current (cf. Figure 7.2 (a)). The third mode carries about 5 % of the information contained in the spatiotemporal data and its amplitude is positive almost always. The corresponding mode seems to account for the modulations in the shape of the clusters.

A different scenario becomes apparent in the case of the 2-PC of type II, whose analysis is depicted in Figure 7.10 (b). The most important mode here is the homogeneously oscillating one, which contributes with ca. 63 % to the full data. The second mode accounts for the clustered structure and its amplitude is similar to the local time series of the inhomogeneous part of the interfacial potential depicted above in Figure 7.5 (c). Similarly to the case of the type I, the third mode shown in Figure 7.10 (b) also seems to account for the modulations in the shape of the clusters.

Original and reconstructed spatiotemporal data are depicted in Figure 7.11 for the 2-PCs of type I, plate (a), and of type II, plate (b). The percentage given for each plot of the reconstructed data represents the cumulative eigenvalues reached.

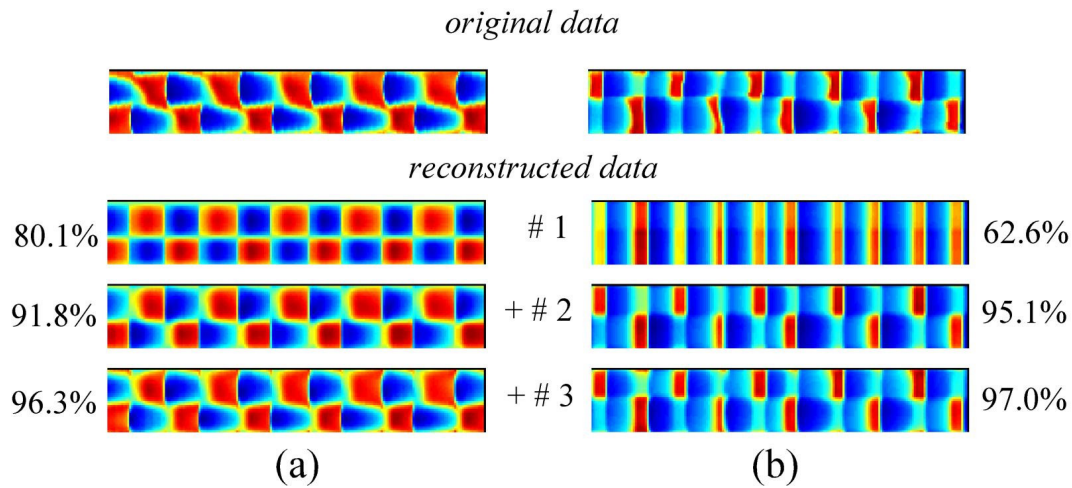


**Figure 7.11:** Spatiotemporal data corresponding to the 2-PC of (a) type I, and (b) type II, depicted in Figures 7.2 (b) and 7.4 (j), respectively. Shown are the original data and the data reconstructed with 1, 2 and 3 modes, respectively.

As anticipated in the previous paragraph, comparing the data reconstructed with the first mode in cases (a) and (b) it becomes clear that the homogeneously oscillating mode plays a more important role in the dynamics of the 2-PCs of type II than the ones of type I. Hence, the presence of a quiescent period and the prominent contribution of the homogeneously oscillating mode are particular features of the 2-PC of type II.

At  $R_c/R_\Omega \approx 0.5$  two types of irregular clusters (ICs) were observed. At the lowest applied voltage investigated, first one of the two domains of the 2-PC of type II discussed above splits into two smaller clusters that oscillates with larger amplitude. In spite of the localized character of the first type of irregular clusters reported here for  $R_c/R_\Omega \approx 0.5$ , they differ from the localized clusters previously reported [199], in which a larger domain without clusters remains nearly homogeneous during the oscillations. Increasing the applied voltage the number of smaller clustered domains increases. Finally, the larger remaining domain disappears, and only small clustered domains survive at high applied voltages. This second type of irregular clusters is characterized by the presence of oscillatory domains, which change their sizes and locations randomly; similarly to the ones reported by Epstein and coworkers [199].

Stronger NGC leads to a stabilization of the ICs, and highly ordered periodic motion is observed at higher applied voltages. More specifically for  $R_c/R_\Omega \approx 0.6$ , five-phase clusters (5-PCs) were observed. Each of the five individual clusters stays at a fixed position and oscillates five times more slowly than the global current. To the best of the author's knowledge, no 5-PC have been observed before.

Predominantly in the case of 2-PCs and ICs a very interesting dynamics of the phase fronts separating different domains was observed. It was shown that stationary (or Ising) fronts evolve into moving (or Bloch) fronts when the smaller domain falls below a critical size. During the motion, the smaller domain tends to expand and the fronts become stationary when the sizes of the two domains are again approximately equal. Simulations by Yang *et al.* [190] on the Belousov-Zhabotinsky reaction with photochemical global feedback have revealed that in the case of 2-PC usually the nodal lines drift during the initial transient period until phase balance is attained. Another interesting feature in the experiments reported in this chapter was the asymmetry observed in the oscillation amplitude of different domains in the absence of phase balance between them.

As a whole, the cluster-cluster bifurcations observed here show remarkable resemblance with some scenarios recently observed in another systems. In a series of papers, Hudson *et al.* (see [201] for a review) have studied pattern formation in reaction-migration systems under global constraint. These studies have been carried out with an array of individual electrodes whose behavior is approximately identical to a single, continuous electrode of the same size as the sum of the individual electrodes [202, 203]. The authors have provided experimental evidence of clustering due to global coupling in populations of periodic [204] and chaotic [205] oscillators. In ref. [204] they observed that upon increasing the global coupling strength, the initial tendency to synchronize the electrodes is lost and an irregular behavior including intermittent clustering is observed. Cluster synchronization is found again under still stronger global coupling.

Epstein and coworkers observed interesting transitions in the Belousov-Zhabotinsky reaction with a photochemical global feedback [198-200]. When increasing the strength of the (negative) global feedback, the authors found the following sequence: 2-PC→3-PC→IC→LC [198-200], where LC stands for localized clusters consisting of spatially fixed oscillatory anti-phase domains that cover only part of the medium, whereas the remaining area stays nearly homogeneous [199].

Clusters were also found by Plenge [129] using a spatially extended version of the homogeneous model describing the hydrogen oxidation reaction in the presence of electro-sorbing ions [53] mentioned in chapter 2. Examples of two and three phase clusters obtained in this study are given in Figures 7.12 (a)–(b) and (c)–(d), respectively.

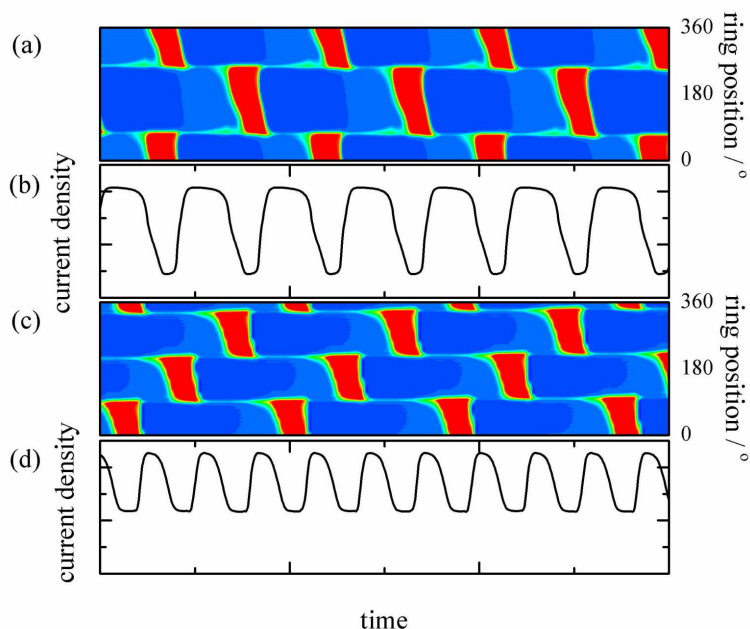


**Figure 7.12:** Simulated two and three phase cluster patterns. (a) and (c): Spatiotemporal evolution of the interfacial potential, (b) and (d) corresponding global current time series. The model used is a spatially extended version of the one describing the oscillatory dynamics of the HOR in the presence of  $\text{Cl}^-$  and  $\text{Cu}^{2+}$  [53]. In this example  $R_c/R_\Omega = 0.90$ . For details see ref. [129].

The simulated results depicted in Figure 7.12 were carried out under strong NGC and the observed 2-PCs and 3-PCs coexisted at the same parameter range. As pointed out by Plenge [129], it is noteworthy that the fronts separating the clustered regions were never stationary but traveled with a constant velocity.

When comparing the simulated cluster patterns depicted in Figure 7.12 with the experimental results shown in this chapter, two main aspects should be emphasized. First, the corresponding current time series given in Figures 7.12 (b) and (d) are relaxation-like, and the spatiotemporal pattern accompanying the high current excursion is characterized by a nearly homogeneous distribution just as the quiescent intervals mentioned above. This feature clearly corresponds to the 2-PCs of type II. Second, considering the presence of Bloch fronts in the simulated clusters, it seems plausible to infer that, farther away from the nonequilibrium Ising-Bloch bifurcation (i.e., the bifurcation that gives rise to the instability

underlying the traveling fronts) [206-209] a further increase of the front velocity could deform the shape of the clusters in such a way that it would connect the borders between different domains. In the case of the 3-PC depicted in Figure 7.12 (c), this ‘cluster distortion’ could give rise to a motion similar to the pulse shown above in Figure 7.9. Therefore, this scenario supports the hypotheses that the pulse in Figure 7.9 is intrinsically different from the ones previously reported in reaction-migration systems (see refs. [43, 47, 150, 187] and also chapters 6 and 8) in the sense that it indeed results from a continuous transition from cluster-like structures experimentally observed for stronger NGC conditions. In addition, 3-PC have experimentally been also observed at lower copper concentration [210].

## 7.2 EXPERIMENTS AT HIGH COPPER CONCENTRATIONS

Results obtained at higher copper concentrations are presented in this section. Two different copper concentrations, namely 0.025 mM [47] and 0.05 mM, are considered. As already mentioned, in the absence of NGC, simple spatially modulated oscillations (MOs) have been observed for copper concentrations higher than 0.01 mM in the entire  $U$  range. In this section, the effect of the NGC on the dynamics of systems with higher copper concentrations will be discussed.

Differently from the case at lower  $[Cu^{2+}]$  discussed in the previous sections, no stable clustered states were observed at the higher  $[Cu^{2+}]$  investigated. Besides the MOs, the main patterns observed here were *target patterns* (TPs), their *asymmetric* variants (A-TPs), and pulses.

The sequence: MOs  $\rightarrow$  (A)-TPs  $\rightarrow$  Pulses for increasingly NGC strength has been observed by Grauel *et al.* [47] for an intermediate copper concentration of 0.025 mM. Figure 7.13 illustrates the TPs and A-TPs observed for  $R_c/R_\Omega \approx 0.3$ . For higher  $U$  values and stronger NGC pulses prevail.

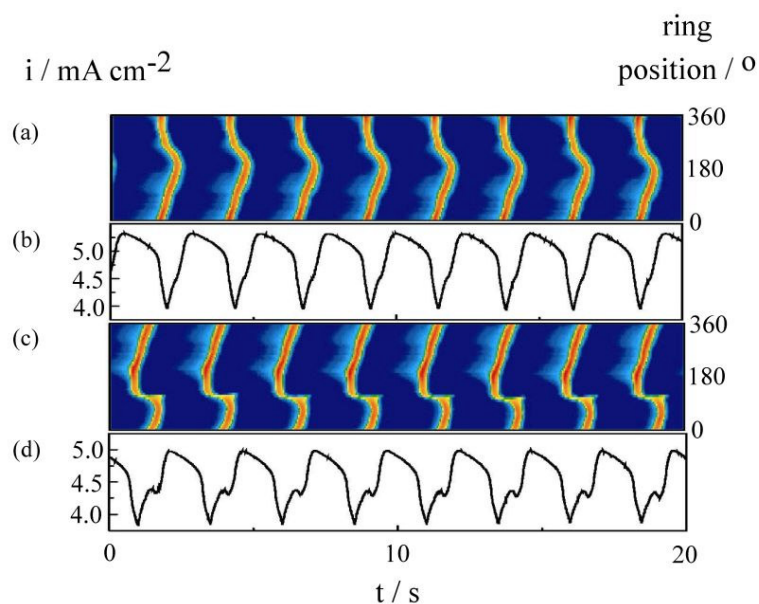


**Figure 7.13:** (a) and (c): Spatiotemporal evolution of the interfacial potential,  $U_{PP}$ , as a function of the ring position and time; (b) and (d): Current time series. Applied voltage  $U$ : (a) and (b): 1.5 V, (c) and (d): 1.37 V. In these experiments a RE mounted in a Haber-Luggin capillary was used and symmetrically placed 15 mm away from the WE. Under these conditions  $R_c/R_\Omega \approx 0.3$ . 0.5 mM  $\text{H}_2\text{SO}_4$ , 0.1 mM HCl, and 0.025 mM  $\text{CuSO}_4$  saturated with  $\text{H}_2$ . After Grauel *et al.*[47].

The one-dimensional target pattern [47, 211] shown in Figure 7.13 (a) is described as a wave source (placed at  $0^\circ$  or  $360^\circ$  in Figure 7.13) emitting two pulses that travel in opposite directions around the ring, meet and disappear at a point symmetrically opposed to the wave source (at about  $180^\circ$  in Figure 7.13 (b)). As is seen in Figures 7.13 (a) and (b), the waves are emitted from the source point during the current decrease and are annihilated during the passive to active transition. The slower relaxation in the active state corresponds to an almost homogeneous interfacial potential distribution along the ring. The presence of these source and annihilation points during the fast current transitions represents a striking similarity between TPs and MOs. This fact has been pointed out by Plenge [129] who emphasizes the continuous nature of the transition from MOs to TPs and suggests a more quantitative way of measuring the overall inhomogeneous character of each pattern. The asymmetric variant of the target patterns (A-TP) is very similar to TP, but one of the two emitted waves stops propagating at a fixed position (at around  $100^\circ$  in Figure 7.13 (c)) shortly after its emission and is annihilated when the wave emitted to the other direction reaches this point.

The influence of the NGC for a copper concentration of 0.05 mM and otherwise identical conditions compared to the ones discussed in the previous sections is summarized in the  $R_c/R_\Omega$  versus  $U$  diagram in Figure 7.14. No homogeneous oscillations were observed, and the lines denote the borders of the oscillatory region. Colored horizontal bars indicate the voltage region in which a certain pattern was observed.

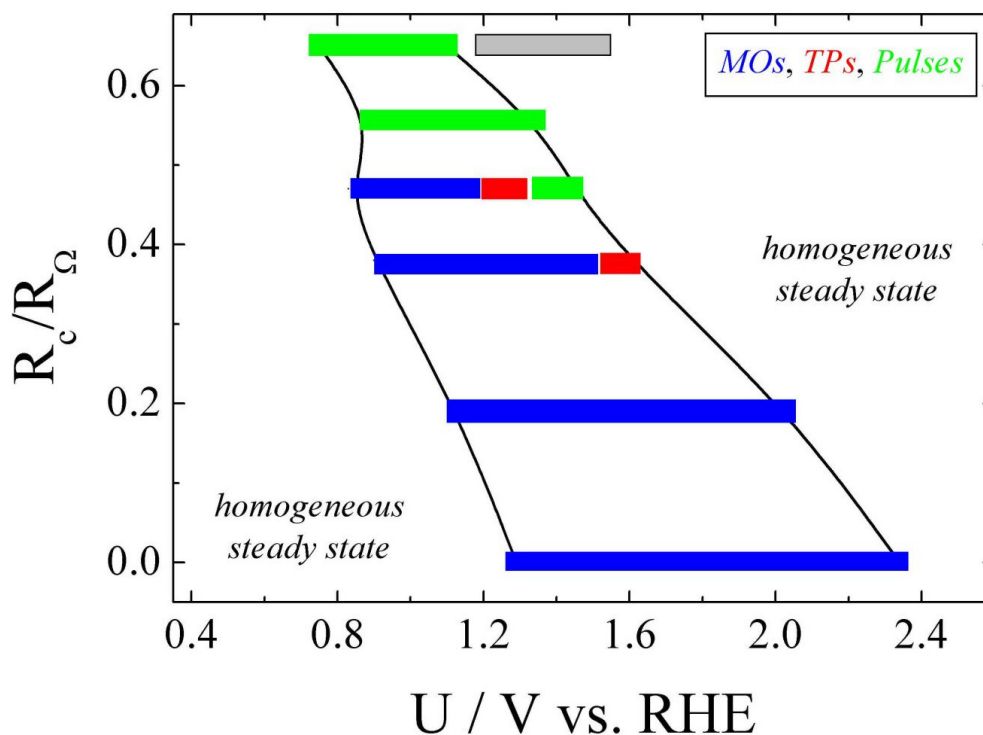


**Figure 7.14:**  $R_c/R_\Omega$  versus  $U$  diagram for the different spatiotemporal patterns observed in the  $\text{Pt}|\text{H}_2\text{SO}_4, \text{Cl}^-, \text{Cu}^{2+}|\text{H}_2$  system at higher copper concentration. MOs: modulated oscillations; TPs: target patterns. Electrolyte: 0.5 mM  $\text{H}_2\text{SO}_4$ , 0.1 mM  $\text{HCl}$ , and 0.05 mM  $\text{CuSO}_4$  saturated with  $\text{H}_2$ . The gray bar marks a region in which so-called *trapped oscillations* were observed (see chapter 8).

At low NGC strength MOs prevail over the entire voltage window. Increasing the strength of the NGC, target patterns (TPs, see below) were found at high  $U$  and  $R_c/R_\Omega \approx 0.38$ . At  $R_c/R_\Omega \approx 0.47$ , MOs, TPs and pulses were observed in this sequence when increasing the applied voltage. For stronger NGC, pulses were observed in the entire oscillatory region, and at  $R_c/R_\Omega \approx 0.65$ , the gray bar marks a region in which so-called *trapped oscillations* were observed. These patterns result from a different mechanism that includes the participation of platinum oxide and will be discussed in the next chapter. It should be mentioned that A-TPs

has been also sporadically observed in the same parameter region, indicated in Figure 7.14 in which TPs were observed.

Additionally to the 2- and 3-PCs mentioned in the previous sections, all spatiotemporal patterns experimentally observed at higher copper concentrations and illustrated in the diagram shown in Figure 7.14 were also captured in realistic simulations by Plenge [129]. Examples of simulated TPs and A-TPs are depicted in Figure 7.15. The observation of simulated A-TPs is a strong hint that the point of propagation failure results from the dynamics itself, rather than from a surface inhomogeneity at this specific point. An almost one-to-one resemblance is observed between simulated (Figure 7.15) and experimentally obtained (Figure 7.13) patterns.

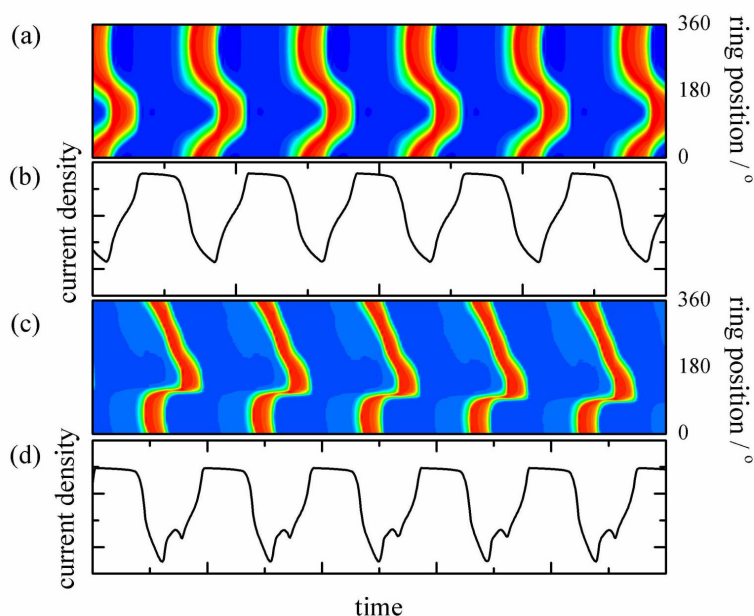


**Figure 7.15:** Simulated target and asymmetric target patterns. (a) and (c): Spatiotemporal evolution of the interfacial potential, (b) and (d) corresponding global current time series. The model consisted of an extended version of the one describing the oscillatory dynamics of the HOR in the presence of  $\text{Cl}^-$  and  $\text{Cu}^{2+}$  [53]. In this example  $R_c/R_\Omega = 0.90$ . For details see ref. [129].

The contribution of the homogeneous mode to the overall dynamics is an important way of differentiating and classifying the observed patterns. In general terms, the smaller this contribution is, the stronger is the spatial symmetry breaking. Taking the example of the MOs, it was shown in chapter 5 that it consists basically of spatial modulations accompanying the steep transitions of the homogeneous oscillating mode in such a way that

the interfacial potential remains spatially homogeneous during most of the oscillatory cycle. On the other hand, the case of traveling pulses implies the existence of a permanent symmetry broken state. Between these two extreme cases, the observation of (A)-TPs illustrates the intermediate case in which spatial symmetry breaking is observed not only during the active to passive and passive to active current transitions as in the case of MOs but also between these two transitions. It means that a more pronounced spatial symmetry breaking is observed in the case of (A)-TPs than in the case of MOs. Moreover, just as for MOs, in the case of (A)-TPs there is a quiescent interval in which no spatial symmetry breaking is apparent in the potential distribution along the electrode (see Figures 7.13 and 7.15).

As shown in Figure 7.14, the MOs→(A)-TPs→Pulses sequence is observed both in the vertical direction towards stronger NGC and also in the horizontal axis for increasing the applied voltage at  $R_c/R_\Omega \approx 0.47$ . In the first case, the transition in the vertical direction can be explained by the desynchronizing character of the NGC which favors the occurrence of anti-phase dynamics [42, 43, 47, 78, 129, 187] and therefore the formation of symmetry broken states. The second transition driven by the applied voltage follows the trend observed in chapter 5 in the sense that symmetry broken states are favored at high applied voltages. It should also be noted that this transition is somewhat different from the one obtained in simulations [129]. A deeper understanding of why a larger applied voltage favors the occurrence of spatial structures is still missing.

### 7.3 SUMMARY

In this chapter the effect of the negative global coupling (NGC) on the oscillatory  $\text{Pt|H}_2\text{SO}_4, \text{Cl}^-, \text{Cu}^{2+}|\text{H}_2$  system using different copper concentrations was presented. The first set of results was obtained using concentrations that were identical to those in the system presented in chapter 5, which was shown to undergo a transition into a turbulent regime when subjected only to the migration coupling. Even for the lowest strength of the NGC studied in this chapter, turbulence was suppressed and clustered patterns were observed at high voltages. Increasing the strength of the NGC, a variety of cluster-like patterns including two different types of two-phase clusters, irregular clusters, and five phase clusters were obtained. For the strongest NGC studied modulated traveling pulses were observed. The author is not

aware of other experimental observation of highly periodic five phase clusters resulting from a global constraint.

For higher copper concentrations the sequence MOs→(A)-TPs→Pulses was found at  $[\text{Cu}^{2+}] = 2.5$  and 5 mM. This sequence appears both for increasing NGC and increasing applied voltage at moderate strength of the NGC. In the first case, the transition has been related to the anti-phase feature induced by the NGC, which increases with its strength. In the second situation however the question of why an increase of the applied voltage favors the MOs→(A)-TPs→Pulses transitions remains unanswered so far.